Bio-Design and Manufacturing (2024) 7:413–427
https://doi.org/10.1007/s42242-024-00293-3

RESEARCH ARTICLE

A mixed-coordination electron trapping-enabled high-precision touch-sensitive screen for wearable devices

Xi Zhang[1,4] · Junchi Ma[1] · Hualin Deng[1] · Jinming Zhong[1] · Kaichen Xu[2] · Qiang Wu[3,4] · Bo Wen[1,4] · Dongfeng Diao[1]

Received: 11 October 2023 / Accepted: 17 May 2024 / Published online: 10 July 2024

Abstract

Touch-sensitive screens are crucial components of wearable devices. Materials such as reduced graphene oxide (rGO), carbon nanotubes (CNTs), and graphene offer promising solutions for flexible touch-sensitive screens. However, when stacked with flexible substrates to form multilayered capacitive touching sensors, these materials often suffer from substrate delamination in response to deformation; this is due to the materials having different Young's modulus values. Delamination results in failure to offer accurate touch screen recognition. In this work, we demonstrate an induced charge-based mutual capacitive touching sensor capable of high-precision touch sensing. This is enabled by electron trapping and polarization effects related to mixed-coordinated bonding between copper nanoparticles and vertically grown graphene nanosheets. Here, we used an electron cyclotron resonance system to directly fabricate graphene–metal nanofilms (GMNFs) using carbon and copper, which are firmly adhered to flexible substrates. After being subjected to 3000 bending actions, we observed almost no change in touch sensitivity. The screen interaction system, which has a signal-to-noise ratio of 41.16 dB and resolution of 650 dpi, was tested using a handwritten Chinese character recognition trial and achieved an accuracy of 94.82%. Taken together, these results show the promise of touch-sensitive screens that use directly fabricated GMNFs for wearable devices.

✉ Bo Wen
drbowen@szu.edu.cn

1 Guangdong Provincial Key Laboratory of Micro/Nano Optomechatronics Engineering, College of Mechatronics and Control Engineering, Shenzhen University, Shenzhen 518060, China

2 State Key Laboratory of Fluid Power and Mechatronic Systems, School of Mechanical Engineering, Zhejiang University, Hangzhou 310058, China

3 Shenzhen University General Hospital, Shenzhen 518055, China

4 Research Center of Medical Plasma Technology, Shenzhen University, Shenzhen 518060, China

Graphic abstract

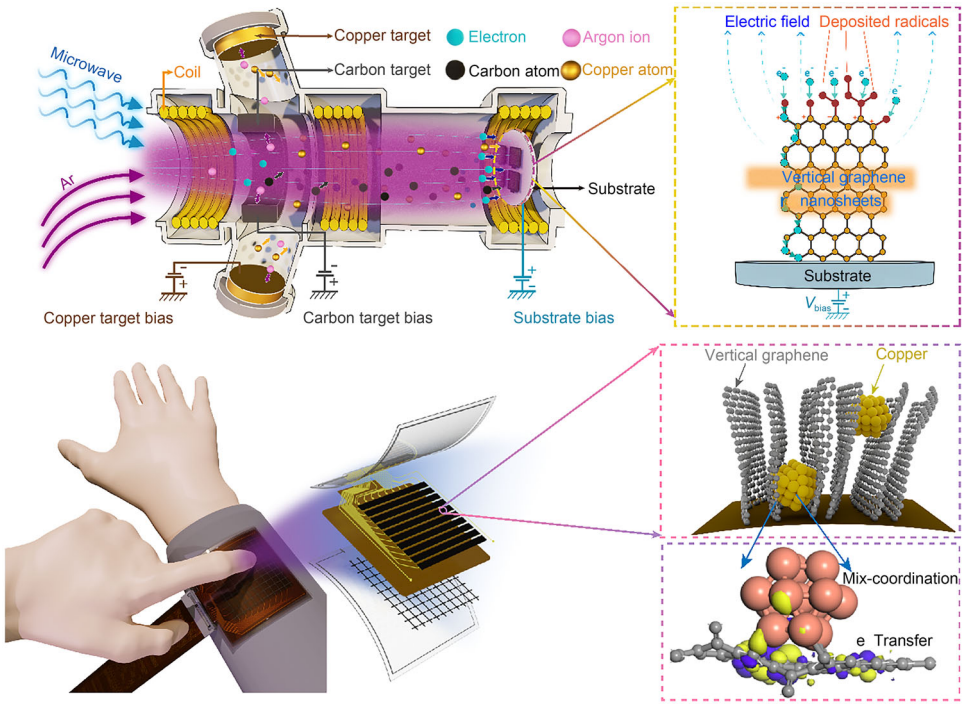

Keywords Flexible touch-sensitive screen · Graphene–metal nanofilms · Mixed coordination · Wearable device

Introduction

With increased growth of wearable devices, touch sensors are becoming popular interface devices for human–computer interaction systems and diverse other applications [1–3]. Touch-sensitive screens can be implemented using various approaches, including capacitive, piezoresistive, piezoelectric, and surface acoustic wave implementations, among others [4–7]. Capacitive touch-sensitive screens have the largest market share at present. The sensing materials used in the fabrication of conventional capacitive touch sensors are usually conductive metal oxides, including indium tin oxide and aluminum-doped zinc oxide, among others [8]. However, the fragility and inflexibility of these materials make them unsuitable for contemporary wearable devices, since these drawbacks can lead to unstable performance and inaccurate touch detection under bending stress [9].

Other materials have been reported as alternatives to conductive metal oxides for use in flexible capacitive sensors. Such materials include reduced graphene oxide (rGO) [10], carbon nanotubes (CNTs) [11, 12], MXene [13], and silver nanowires [14–16]. Of these, graphene has attracted extensive research interest due to its desirable physical properties [17–22]. It usually needs to be transferred to a dielectric layer, where it acts as a sensing electrode, before finally being encapsulated into a flexible capacitive sensor with a multilayer structure [23–25]. However, when sensors are deformed by external forces, the mechanical mismatches between dielectric and electrode layers can lead to inaccurate sensing [26]. At the same time, polarized charges need to overcome the poor conductivity of graphene for collection by electrodes, thereby reducing sensor sensitivity [27]. These factors hinder the further development of touch sensors and their potential applications.

Here, we used an electron cyclotron resonance (ECR) system [28, 29] to achieve a one-step (from raw material to device) fabrication process for flexible touch sensors (Fig. 1a). This system sputters atoms of a specific material directly onto the substrate, which ensures that a sensing material could be firmly attached to flexible substrates. At the same time, the graphene–metal nanofilm (GMNF) prepared using this system uses only two low-cost and environmentally friendly materials, copper and carbon, which will significantly reduce the cost and environmental impact of touch sensors. The vertical graphene nanosheet network ensures that the sensing material retains anti-bending properties, and that copper nanoparticles embedded in the vertical graphene nanosheet network (Fig. 1d) form mixed-coordination (Fig. 1e) materials. This generates an electron trapping effect that facilitates efficient electron transport,

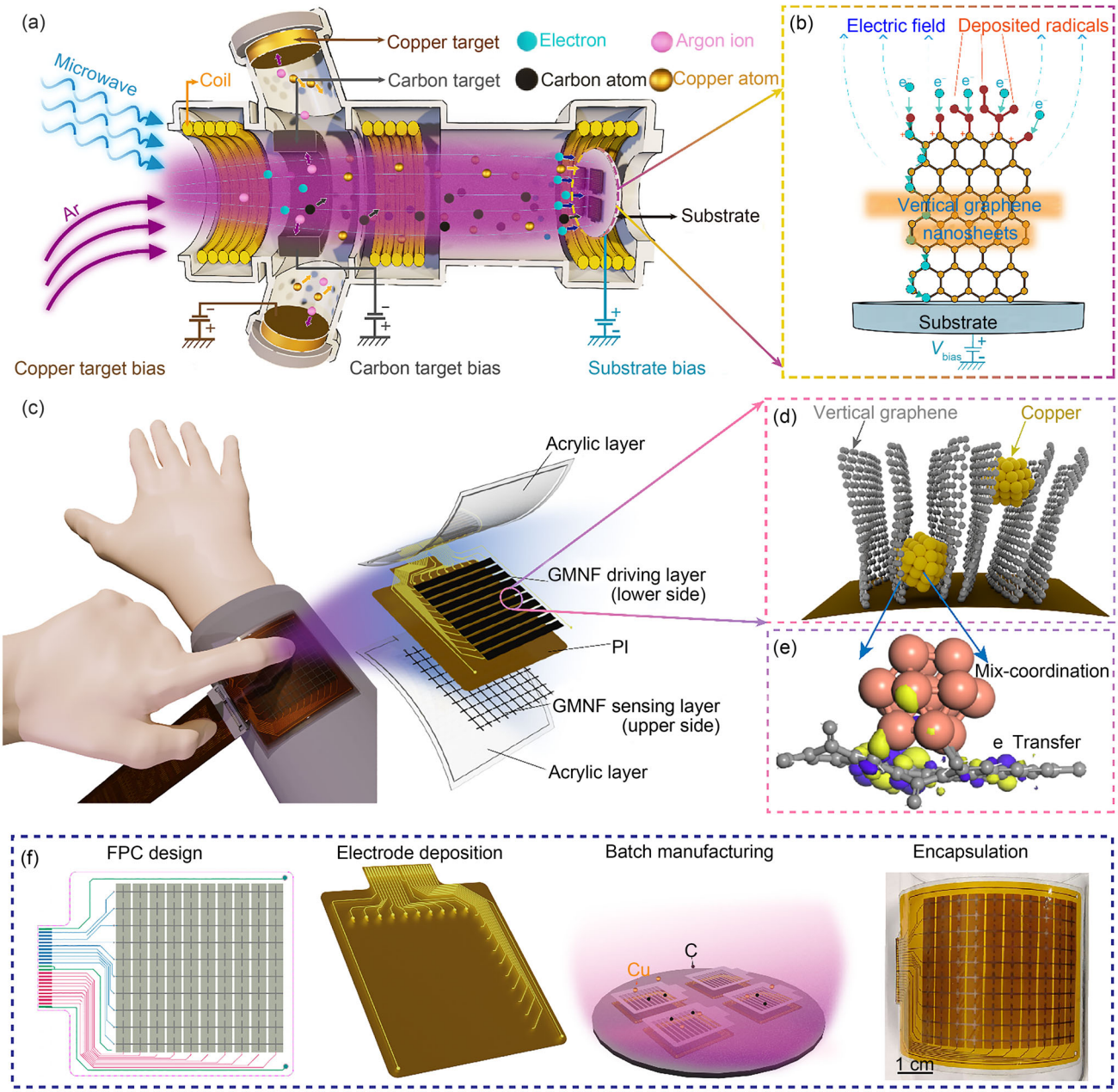

Fig. 1 Overview of the electron cyclotron resonance (ECR) system and an induced charge-based mutual capacitive sensing screen. **a** Schematic illustration of the ECR system. Copper and carbon target biases were applied to sputter copper and carbon onto the substrate. Substrate bias was used to attract electrons and atoms to grow the graphene–metal nanofilm (GMNF). **b** Depiction of the growth process of vertical graphene nanosheets as induced by the ECR system. **c** Demonstration of the five components of the flexible touch-sensitive screen: the top and bottom acrylic protective layers, the GMNF sensing layer, the PI substrate, and the GMNF driving layer. The port of the touch screen was connected to external circuitry using a standard 2.54 mm connection jack. **d** The GMNF is composed of copper nanoparticles and vertical graphene nanosheets. **e** Mixed coordination of the Cu–C material, as calculated using the density functional theory (DFT) method. Purple and yellow clouds show the highest occupied molecular orbitals (HOMOs) of the system, and show the electron transfers within the system that contribute to the sensing of charge redistribution. **f** The fabrication process of the device, which is suitable for batch manufacturing

resulting in high sensitivity for the touch screen [29]. The mixed coordination of Cu–C material is shown in Fig. 1e, as calculated using the density functional theory (DFT) method (Fig. S9 in Supplementary Information). Purple and yellow clouds indicate the highest occupied molecular orbitals (HOMOs) of the system; these data show that electron transfers within the system contribute to charge redistribution sensing. The thickness of the GMNF developed here was only 100 nm, which is much smaller than the thickness of the flexible substrate (80 μm). Due to the firm adhesion of GMNF to

the substrate, the flexible performance of the sensing screen depends entirely on the flexible substrate to achieve a high level of precision. Next, we designed a flexible and interactive touch-sensitive screen platform by attaching the flexible touch-sensitive screen to garments (Fig. 1c). Further testing showed that this system can accurately recognize Chinese characters when written by the user, thereby demonstrating the potential of how a GMNF can be applied to wearable devices. Overall, this study introduces a new approach of leveraging a GMNF to create a novel touch sensor, thereby expanding what is possible in the fields of human–computer interactions and wearable technologies.

Experimental method

Fabrication of GMNF-based touch-sensitive screens

Metal masks (Fig. S1 in Supplementary Information) of the driving and sensing electrodes were fixed to the front and back sides of a polyimide (PI) substrate (thickness: 80 μm) using PI tape. First, the side on which the driving electrodes were located was fixed outwardly relative to the chamber base of the ECR. This was performed under an argon pressure of 4×10^{-2} Pa, and microwaves (power: 500 W) were fed into the vacuum chamber to generate plasma. Ar^+ ions were then sputtered onto the negatively biased carbon target and copper target to produce GMNF on the driving side of the substrate. Next, after waiting for the system to cool down for 20 min, the side on which the sensing electrodes were located was fixed outwardly onto the chamber base of the ECR. Subsequently, the rotary deposition motor was switched on and operated at a speed of 10 r/min. Deposition was carried out under the same conditions as for the deposition process used for the driving electrodes. Thickness was controlled by varying deposition time. The deposition time used in this study was 30 min for a single side, which resulted in a GMNF thickness of approximately 100 nm per side. After deposition, positive bias was applied to the substrate to attract electrons. GMNF nanostructures were then analyzed using Raman spectroscopy (HORIBA, HR-Resolution, HORIBA STEC, Japan; a wavelength of 532 nm), scanning transmission electron microscopy (STEM, FEI Titan Cubed Themis G2 300, Thermo Fisher Scientific, USA), and scanning electron microscope (SEM, FEI Scios, Thermo Fisher Scientific, USA).

Testing of induced charge GMNF-based mutual capacitive sensors

Next, we performed testing of mutual capacitive sensors. To do so, GMNFs were deposited on the upper and lower surfaces of a 2 cm × 2 cm PI with a thickness of 80 μm. This was performed at a substrate bias voltage of 40 V, a copper target current of 700 mA, and a deposition time of 30 min. Next, the GMNFs were encapsulated in an acrylic tape with a thickness of 50 μm to form a mutual capacitive sensor (Fig. S2 in Supplementary Information). The prepared sensor was then fixed on a one-dimensional (1D) moving platform for bending and cycling tests. Subsequently, we fixed the prepared sensor on a two-dimensional (2D) moving platform (Fig. S3 in Supplementary Information) and conducted anti-false-touch tests, touch sensitivity tests, and other sensitivity tests under varying contact conditions and at different heights. To avoid the influence of test subject movements (i.e., shaking of the hand) on experimental results, we used a copper foil with a diameter of 8 mm to contact the device, which was then connected to the human body via a wire. We performed sensitivity tests under different contact conditions by dipping the copper foil in water and by adding gloves to the copper foil, separately.

Touch increment change testing

To test the differences in touch increment, we used two copper foils to encapsulate probes of the 2D moving platform (diameter: 8 mm) that were connected with the human body, and these were used to touch the screen. The contact center of one copper foil was located at the center of the intersection area of the fourth driving electrode and the third sensing electrode, while the contact center of the other electrode was located at the center of the intersection area of the seventh driving electrode and the eighth sensing electrode.

Signal-to-noise ratio (SNR) testing

The experimental conditions used here were consistent with those of touch increment change testing. For SNR testing, the center of the copper foil was placed at the center of the overlapping position of the fifth driving electrode and the fifth sensing electrode. To test temperature stability, the flexible touch screen was attached to a heating platform, and the heating platform was then heated to 30, 40, 60, 80, and 100 °C. At each temperature, nine touch points were taken evenly on the surface of the touch screen.

Results and discussion

Preparation of the touch-sensitive screen

An ECR system uses microwaves to induce the formation of stable plasmas, uses magnetic coils to accelerate electrons, and uses ions to sputter target atoms (Fig. 1a). Unlike magnetron-based sputtering, the plasma generation and sputtering processes are separate in the ECR system [30]. Thus, the performance of the film can be modulated by controlling the parameters of substrate bias, copper target current, and deposition time (Fig. S4 in Supplementary Information). Accordingly, it is possible to transform carbon sources from an amorphous structure to a vertical graphene nanosheet structure (Fig. 1b) by adjusting preparation parameters [28]. The structure of the touch-sensitive screen is shown in Fig. 1c. It is divided into three main parts, i.e., protective layers, induction layers, and substrate layers. The protective layers are comprised of acrylic tape (50 μm) and are divided into upper and lower protective layers. Their function is to insulate the human body from the GMNF. The acrylic tape was selected since it has a good dielectric constant, which facilitates mutual capacitance detection. To create the induction layer, the two electrodes are placed perpendicularly to each other on the two surfaces of the substrate to form a touch-sensitive array. Sensing electrodes are located on the upper surface of the PI substrate and are used to detect signals, while driving electrodes are present on the lower surface of the PI substrate and receive the excitation signal. The surfaces of the driving and sensing electrodes cannot be swapped, or the sensing electrodes will be shielded by the driving electrodes such that the touch signal cannot be detected. GMNF is used as the material for the sensing layer, since it has good electrical conductivity and is difficult to bend. For the substrate layer, GMNFs are firmly adhered to the PI substrate surface by the ECR system.

The flexible printed circuit (FPC) of the flexible touch screen with the encapsulated device is shown in Fig. 1f. The FPC layout of the touch-sensitive screen must follow certain rules to ensure the consistency of the signal, avoid cross talk, and avoid the introduction of unnecessary noise that would prevent the touch screen from working properly. According to these rules [31], all wires were placed on the lower surface of the substrate (i.e., the same surface as the driving electrodes), while the sensing electrodes on the upper surface are connected to the lower surface by vias. The design sizes of the FPC are shown in Fig. S5 (Supplementary Information). The metal masks of the sensing electrodes and driving electrodes were attached to the related substrate and then sent into the ECR system, after which the GMNFs were deposited directly onto the driving and sensing surfaces. This process can reduce defects during manufacturing, and is therefore suitable for batch manufacturing.

Characterization of graphene–metal nanofilms

The ECR system can directly fabricate functional materials on flexible substrates, and is induced by the unique plasma generation mode of ECR and the polariton energy-transfer mode between the plasma and the surface of the substrate. Figure 2a shows the structure of the touch-sensitive screen. A cross-sectional view of these parts obtained via SEM is shown in Fig. 2b. Since a GMNF is only 100 nm thick, it is not visible on this scale. Figure 2c illustrates the structure of a GMNF, and Fig. 2d shows the SEM image of a GMNF. Next, Figs. 2e and 2f show STEM images of GMNF at substrate bias voltages of 0 and 40 V. When using the ECR system, the kinetic energy of electrons can be increased by increasing substrate bias, which permits more electrons to collide with carbon and copper atoms, which in turn results in the deposition of higher density films on the PI substrate. When the number of collisions between electrons and carbon atoms increases, higher energy will be imparted to carbon atoms. This induces bonding between carbon atoms, thereby resulting in the transition of deposited carbon atoms from a disordered amorphous structure to a vertical graphene nanosheet structure [32]. As shown in Fig. 2e, the ordered vertical graphene nanosheet structure is not observed when the bias voltage of the substrate is 0 V. Next, fast Fourier transform (FFT) was performed on the red region; the inset shown in Fig. 2e is the electron diffraction image, which reveals that the object in the red region has a face-centered cubic structure, which corresponds to the structure of copper nanoparticles [33]. This indicates that the ECR system can successfully embed copper nanoparticles onto deposited films. Moreover, when the bias voltage of the substrate was 40 V, we observed that the carbon atoms form a partially ordered structure; the more obviously ordered carbon atoms are marked by yellow circles in Fig. 2f. The FFT of ordered carbon atoms (indicated by the green area in Fig. 2f) yields the results shown in the green inset. Here, significant Laue spots can be observed, and the reciprocal lattice spacing between the spots was 5.78 nm^{-1}, yielding an interplanar distance of d=0.346 nm in this direction. This corresponds to the (0001) surface of multilayer graphene and indicates that the material present in the green area is multilayer graphene [34, 35]. By performing FFT on disordered carbon atoms (i.e., the blue region shown in Fig. 2f), the obtained electron diffraction map has no obvious Laue spots, indicating that the internal structure of this region is generally amorphous. However, Fig. 2f shows that the copper nanoparticles are surrounded by well-ordered vertical graphene nanosheets.

Figures 2g and 2h show the compositional distribution of GMNF. Figure 2g shows a high-angle annular dark-field (HAADF)-scanning transmission electron image of GMNF, with copper shown in white and carbon shown in gray. The two materials are also marked in pink and black dotted lines,

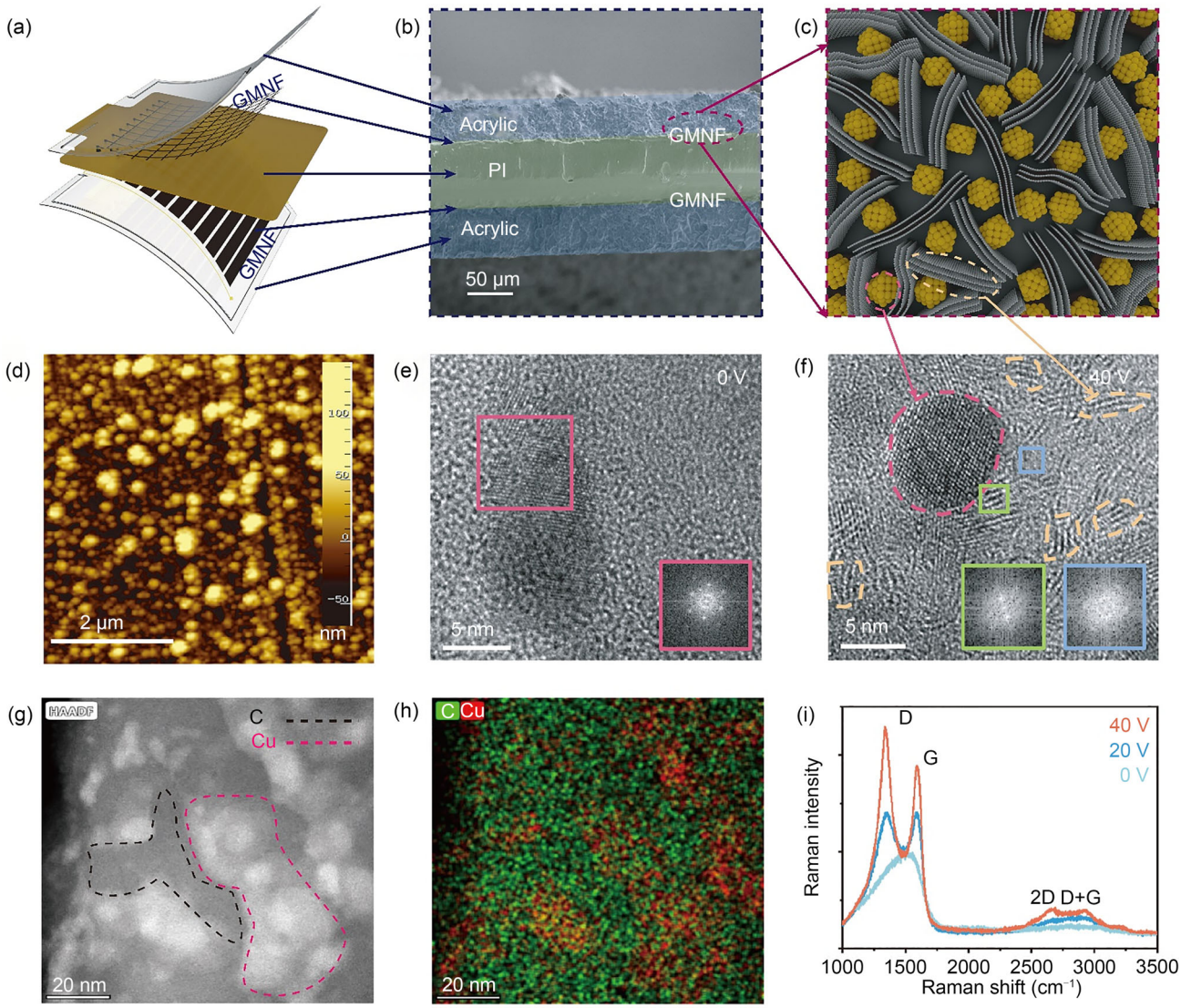

Fig. 2 Characterization of graphene–metal nanofilms (GMNFs). **a** Illustration of the five-layer structure of the flexible touch-sensitive screen: acrylic (protection)-GMNF (driving layer)-PI (dielectric)-GMNF (sensing layer)-acrylic layer. **b** Cross section of the film imaged by scanning electron microscope (SEM). The thicknesses of the acrylic protective layer, GMNF, and polyimide (PI) were 50 μm, 100 nm, and 80 μm, respectively. **c** Illustration of the GMNF structure. Shown are copper nanoparticles and graphene nanosheets. **d** SEM image of a GMNF. Light-colored parts indicate copper nanoparticles, while dark-colored parts indicate graphene nanosheets. **e**, **f** Transmission electron microscope (TEM) images of films under substrate bias voltages of 0 and 40 V. Insets show fast Fourier transform (FFT) images of the selected region (i.e., labeled red, green, and blue). **g** High-angle annular dark-field (HAADF) image of a GMNF. The white part indicates copper and the gray part indicates carbon; these are marked using pink and black dotted lines, respectively. **h** Compositional analysis of region (g). **i** Raman spectra of a GMNF at substrate bias voltages of 0, 20, and 40 V

respectively. Figure 2h shows the result of a composition analysis of the region shown in Fig. 2g; this image shows that the distribution of copper and carbon perfectly corresponds to that shown in Fig. 2g. Specifically, the copper atoms have aggregated into copper nanoparticles, while the carbon is uniformly distributed throughout this region as either an amorphous or a vertical graphene nanosheet structure.

Next, the Raman spectra of the deposited films were tested at substrate bias voltages of 0, 20, and 40 V, as shown in Fig. 2i. When the substrate bias voltage is 0 V, there were no D- or G-peaks, indicating that no graphene nanosheets were present in the deposited film and therefore that the carbon was present in the film in an amorphous form [36]. At a substrate bias voltage of 20 V, we observed obvious D- and G-peaks. However, no 2D peak was observed, indicating that the deposited film contains graphene nanosheets, but their crystallinity was very low. Moreover, the ratio of the D-peak to the G-peak increased from 1.005 at 20 V to

1.218 at 40 V, indicating that the graphene nanosheet content increased. Moreover, 2D peaks can be observed, which indicates both that the crystallinity of graphene nanosheets increases with increasing voltage and that vertical graphene nanosheets of a certain size form within the deposited film.

Testing of induced charge GMNF-based mutual capacitive sensors

The touch-sensitive screen is based on an array of mutual capacitors. The working mechanism of induced charge GMNF-based mutual capacitive sensors is shown in Fig. 3a. The human body can be thought of as equivalent to a circuit model in which a resistor and a capacitor are connected in series to the ground. After applying an excitation signal to the driving electrode of the mutual capacitor sensor, but without touching it, the driving electrode and the sensing electrode will form a capacitor C_{xy}. However, when a finger approaches the capacitor, the electric fields formed between C_{xy} are instead diverted to the ground through the finger, thereby reducing the capacitance of C_{xy}. The touch sensitivity testing circuit is visualized in Fig. S6 (Supplementary Information). We used an analog-to-digital converter (ADC) module to measure changes in touch voltage during the mechanical stability test, and then used it to reflect sensor sensitivity.

With defined electrode shape, adjusting the preparation parameters of the GMNF can modulate the C_t value as shown in Fig. 3a and thus vary the touch sensitivity of the device. We set the parameters of the substrate bias voltage to 10, 20, 30, and 40 V and held the copper target current fixed at 700 mA and the deposition time at 30 min; this allowed us to determine the changes in film square resistance and touch sensitivity in response to different substrate bias voltages (Fig. S4 in Supplementary Information). Furthermore, as the substrate bias voltage gradually rose from 10 to 40 V, the square resistance of the film decreased nearly linearly from 200 to 35 Ω/sq, and the change in touch voltage of the film increased from 69.3 to 217.5 mV. This effect is due to the electron trapping effect of the copper nanoparticles and vertically grown graphene nanosheets formed during mixed coordination, which increases the conductivity of the film. Thus, rising film conductivity helps to establish a stronger electric field. Moreover, the stronger the electric field, the more obvious the interaction between the human body and the electric field, leading to greater change in mutual capacitance (i.e., touch sensitivity). In addition, the higher the film conductivity, the smaller the attenuation of high-frequency signals after they pass through the film.

DFT calculation results for the copper nanoparticle-graphene nanosheet system are shown in Fig. 3b. Numbers 1, 2, and 3 indicate the inner, outer, and mixed-coordination atoms, respectively. The partial densities of states (PDOSs) of atoms labeled 1, 2, and 3 show that the peaks of Cu 3d orbital electrons shifted from deeper energy (approximately −0.15 eV) to upper energy (approximately −0.09 eV) (i.e., d-band center moved closer to the Fermi level E_f). This is known as the polarization effect [37]. Valence band polarization is known to occur with metals; specifically, the valence band redshifts since nonlocal charges are polarized upward to E_f at under-coordinated sites [38]. This effect contributes to charge redistribution sensing transfers observed in the system.

The simulation results obtained using finite element analysis software (COMSOL 6.0) are shown in Fig. 3c. Here, the orange dashed line represents a finger. When the finger approaches the capacitor, the electric field line undergoes a significant transfer [39].

We note that when the PI substrate is bent, the vertical structure of graphene nanosheets tilts to offset some of the bending-induced deformation. Moreover, when the PI substrate expands back, the van der Waals force between the film and PI substrate causes the vertical graphene nanosheets to return from a tilted to a vertical state. Moreover, at a certain bending curvature, the rate of change of graphene resistance is small [40]. Therefore, a GMNF can possess a strong anti-bending property.

Accordingly, here we bent GMNF mutual capacitive sensors by fixing them to a 1D moving platform as shown in Fig. 3d. Next, the bending angle was gradually increased from 0° to 120°, and the resistance was measured by using a source instrument every 5° during the bending process. This allowed us to obtain the curve for the bending angle and resistance change rate. The rate of change of resistance is defined as follows [41]:

$$\frac{\Delta R}{R_0} = \frac{R_1 - R_0}{R_0} \times 100\%, \tag{1}$$

where R_0 is the original resistance value and R_1 is the resistance value in the bent state.

The results of these bending tests are shown in Fig. 3d. They show that as the bending angle increases, the resistance change of the sensor increases linearly. However, when the bending angle reached 120°, the change in resistance was still only 6.32%, indicating that the sensor maintained good electrical conductivity across a range of bent conformations. This is a prerequisite for the preparation of a flexible mutual capacitive touch-sensitive screen, since it ensures that the sensor can work stably when bent.

Next, a repeated bending test was conducted on the sensor. Thus, we bent it 3000 times using a 1D moving platform, each time at an angle of 90°. Every 50 times, we recorded the change in touch voltage. These results are visualized in Fig. 3e. Briefly, no significant differences in touch sensitivity were observed after bending, and the touch sensitivity did

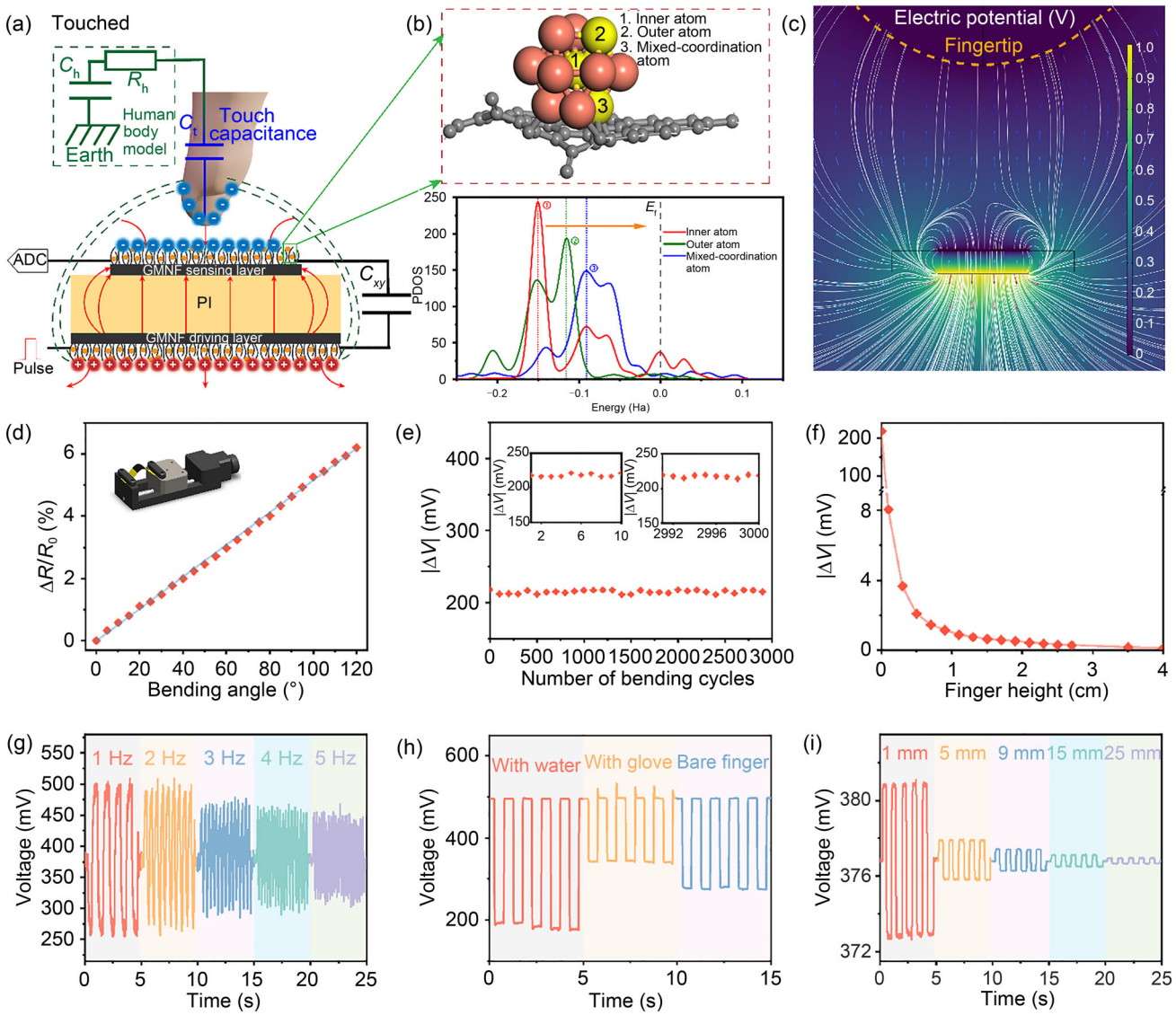

Fig. 3 **a** Mechanistic diagram of induced charge-based mutual capacitive sensors. Testing was performed by applying an excitation signal to the graphene–metal nanofilm (GMNF) driving electrode and by measuring voltage fluctuations through the analog-to-digital converter (ADC). **b** Density functional theory (DFT) calculation results for the copper nanoparticle-graphene nanosheet system. The numbers 1, 2, and 3 indicate inner, outer, and mixed-coordination atoms, respectively. The partial density of state (PDOS) polarization effect calculated by DFT for atoms labeled 1, 2, and 3 is shown in the lower panel. **c** Simulation of the electric field distribution. As the finger approaches, a change in the distribution of electric field lines occurs, and this causes redistribution of the induced charge. **d** Bending angles of induced charge-based mutual capacitive sensors and associated resistance change ratio curves. These results show that when the sensor is bent to 120°, the ratio of resistance change is 6.32%. The inset shows the 1D test platform. **e** Touch sensitivity of the sensor after repeated bending movements. Insets show the results of the initial and final 10 repetitions of the bending test. **f** Results of the anti-false-touch test. As the finger moves away, the touch sensitivity showed an exponential decrease. **g** Touch sensitivity at different touch frequencies, demonstrating sensor responsiveness. **h** Touch sensitivity test at 1 Hz under different contact conditions (i.e., with a wet hand, while wearing gloves, and using a bare finger). **i** Touch sensitivity obtained at a frequency of 1 Hz at heights of 1, 5, 9, 15, and 25 mm; shown are values for 0.5 mm raised, and 0.5 mm lowered

not deteriorate, remaining at about 215 mV even after 3000 bending cycles.

The sensor was also tested against "mis-touches." We found that as the distance between a copper foil (used here as a substitute for a finger) and the sensor decreased, the sensing voltage of the sensor varied exponentially (Fig. 3f). When the copper foil touched the sensor, the touch voltage change suddenly increased to 217 mV, which is two orders of magnitude higher than 8 mV.

Next, we tested the stability of the sensor under different states. In general, the sensor was found to be able to generate distinct touch voltage changes at different touch frequencies,

thereby demonstrating the high responsiveness of the GMNF capacitive sensor (Fig. 3g). Furthermore, in tests simulating three daily scenarios (i.e., using a wet hand, wearing gloves, and using a bare finger), we found that the sensor was able to accurately recognize all forms of touch and to generate a clear change in voltage (Fig. 3h). This indicates that the sensor can be used in real-world situations. Moreover, when repeatedly approaching the sensor at different heights, the touch voltage changes measured from the touch-sensitive screen significantly decreased as the contact distance increased (Fig. 3i). This result corresponds to Fig. 3f and indicates that the sensor can prevent accidental touches and has some potential for being operated without touching.

GMNF touch-sensitive screen test

Mutual capacitive touch screens detect changes in capacitance between driving and sensing electrodes. After encapsulation, we used the SAM D21 Xplained Pro development board to test the signal stability of the touch-sensitive screen. We also used it as the lower computer of our interactive system (Fig. S7 in Supplementary Information). Here, the system determined whether a touch action occurred by detecting a touch increment (touch delta). When inputting the same excitation signal to all driving electrodes, the signal change of all sensing electrodes was detected [42]. Moreover, if the electrode to which the excitation signal is applied is the same as the driving electrode of the touch point, the signal change at the sensing electrode of the touch point will be at the maximum, and the X and Y coordinates of the touch point can be identified. As shown in Fig. 4a, when the excitation signal is applied to the X_5 electrode, the maximum signal change is detected at the Y_5 electrode, and these touch coordinates are written here as (X_5, Y_5).

We therefore collected touch increment ("touch delta") data from all sensing electrodes when driving all driving electrodes. The post-processing results are shown in Fig. 4b. Here, we can see that there are two distinct touch points over the whole touch plane, i.e., points (4, 3) and (7, 8). This result verifies the hypothesis that the GMNF mutual capacitive touch-sensitive screen has the ability to detect multiple touched points.

The SNR reflects the amount of noise in the touch detection system. In general, the higher the SNR, the higher the accuracy of the touch coordinates reported by the system. The SNR is calculated using the following equations [43]:

$$\text{Signal} = \text{Touchdelta}_{\text{AVG100}} - \text{Untouch}_{\text{AVG100}}, \tag{2}$$

$$N_{\text{RMS100}} = \sqrt{\frac{\sum_{n=0}^{99}(\text{Touchdelta}[n] - \text{Touchdelta}_{\text{AVG100}})^2}{100}}, \tag{3}$$

$$\text{SNR [dB]} = 20\lg\frac{\text{Signal}}{N_{\text{RMS100}}}, \tag{4}$$

where Touchdelta is the touch increment, Untouch is the value detected by the system when there is no touch, and the subscript "AVG100" means the average value of 100 technical replicate measurements.

When the fifth driving electrode is driven, signals from all sensing electrodes are acquired at 100 points without touching and at 100 points with touching. These results are shown in Fig. 4c. Moreover, the touch increment is about 33.91 mV and the detection value when untouched is about 1 mV. According to Eq. (4), the SNR is 42.7 dB. Next, we sampled nine points uniformly distributed throughout the plane of the flexible touch screen and found a mean SNR value of 41.16 dB.

Resolution refers to the ability of the touch detection system to detect small changes in touch coordinates. The equation for calculating resolution is as follows [44]:

$$\text{Resolution} \cong 3.32 \times \left(\lg \text{electrodes}_{\text{num}} + \lg \text{Touchdelta}_{\text{AVG100}} - \lg \text{noise}_{\text{pk-pk}}\right), \tag{5}$$

where Resolution is expressed in "bits," $\text{electrodes}_{\text{num}}$ is the number of electrodes along this axis, and $\text{noise}_{\text{pk-pk}}$ is the maximum value of the touch increment minus the minimum value of the touch increment.

From the data shown in Fig. 4c, the values for these parameters were as follows: $\text{Touchdelta}_{\text{AVG100}}$=33.83 mV, $\text{noise}_{\text{pk-pk}}$=2, $\text{electrodes}_{\text{num}}$=10. Thus, the resolution of the touch detection system reported here is 7.4. In practice, the resolution of the flexible touch film is set to 7; that is, the maximum value that can be represented by the XY coordinates using this system is 2^7=128. The actual sensing area of the flexible touch film is 50 mm×50 mm, and therefore, the smallest change in distance that the system can detect along the X- or Y-axis is 0.39 mm (i.e., corresponding to a resolution of 650 dpi). The resolution of this touch screen is greater than 150 dpi, which indicates that it is highly sensitive and has low noise.

Next, we used a 2D moving platform to take 19 linear measurement points uniformly from coordinates (0, 0) to (127, 127) to touch the screen at these points. We then compared these set points to the set of coordinates reported by the system. These results are shown in Fig. 4d and show a linearity (R^2=0.91) for the system as a whole.

The response time of the touch-sensitive system was also tested. Each driving electrode has a scan time of 2 ms, and 10 driving electrodes were used in total. Thus, the time to collect a frame of data is 20 ms. Figure 4e shows the touch increments of a sensing electrode. Here, the time interval between each point is 25 ms, and a touch event is detected

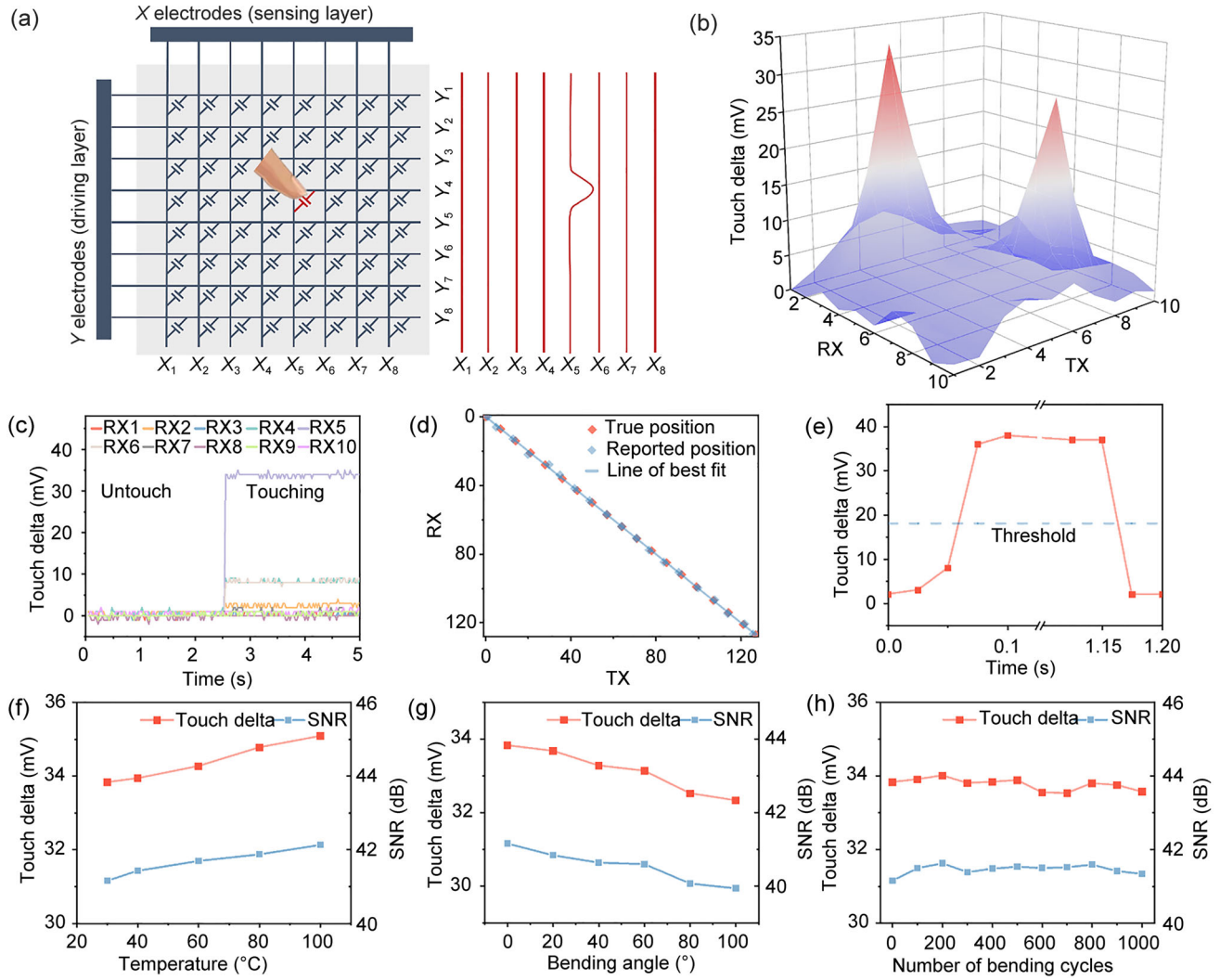

Fig. 4 **a** Illustration of the working principle of the touch-sensitive screen, which is based on an array of mutual capacitors. Briefly, a mutual capacitance is formed between two electrodes, e.g., *X* and *Y*. When an excitation is applied to the *Y* electrodes (i.e., the driving layer) and a finger touches the *X* electrode (i.e., the sensing layer), the resulting voltage change is highest at the point of touch. **b** Touch increment map for the touch film when touching points (4,3) and (7,8). The touch increment is the change in voltage detected by the microcontroller when a finger touches the screen. It is caused by the finger forming a circuit with the earth to release the charge. **c** Sampling data of the touch-sensitive system after touching and untouching 100 points, separately. Touching the fifth sensing electrode (RX5) above the fifth driving electrode generated the greatest touch increment change relative to the other sensing electrodes. **d** Accuracy test of the touch-sensitive system. The touch points reported by the system and the true touch points were on a straight line after fitting. **e** Response time of the touch-sensitive system. We set the touch threshold to 50% of the touch increment to determine whether a touch action occurred or not. **f**–**h** Touch increment and signal-to-noise ratio (SNR) of the touch-sensitive system under different temperatures, at different bending angles, and following repeated bending cycles

when the touch increment is greater than the threshold. Moreover, when the touch signal disappears, the system responds within 25 ms.

The signal stability of a touch-sensitive screen refers to the ability of the touch detection system to function properly under different operating conditions. Here, the signal stability of the flexible touch films was tested under different operating conditions as follows. (i) Temperature stability. To examine temperature stability, a flexible touch-sensitive screen was attached to a heating platform, and the temperature of the heating platform was raised to 30, 40, 60, 80, or 100 °C. Nine touch points were uniformly triggered using the touch film at each of these temperatures, and the maximum touch increment and the SNR were calculated each time. The results shown in Fig. 4f indicate that as the temperature increased, the touch increment gradually increased from 33.83 mV (at 30 °C) to 35.09 mV (at 100 °C). This occurs because higher temperatures increase the kinetic energy of

electrons flowing inside the GMNF. This means that the vertical graphene edges are able to capture the electrons more quickly, leading to an increase in the conductivity of the film and consequently an increase in touch increment [45–47]. The SNR changes along with the touch increment according to the relationship indicated in Eq. (4); thus, its value also increased gradually with temperature, from 41.16 dB at 30 °C to 42.13 dB at 100 °C. (ii) Bending stability. In general, as the bending angle increases, the touch increment decreases. As shown in Fig. 3d, the resistance of the film decreased linearly when we increased the bending angle; furthermore, when the bending angle of the film reached 120°, the resistance had decreased by 6.32% relative to the original (i.e., unbent) value. As shown in Fig. 4g, when the bending angle increased, the touch increment of the system decreased from 33.83 to 32.33 mV and the SNR decreased from 41.16 to 39.94 dB. These results suggest that when the bending angle reaches 100°, the film still has a good electrical conductivity, and the detection system can still maintain a high SNR. (iii) Cyclic bending stability. The results of cyclic bending tests are shown in Fig. 4h. These results show that the performance of the system did not deteriorate after repeated bending, retaining the consistency of the unbent film. Taken together, the results of these three tests show that the touch screen device reported here can remain in stable working condition under strenuous testing environments.

Handwritten Chinese character feature extraction

Figure 5a displays raw data collected for writing of the Chinese character "ah." Here, the different colored dots represent different strokes, and each stroke refers to the set of coordinates captured by the system from the time a finger touches the touch screen to the time it leaves the touch screen. Here, we needed to preprocess handwritten Chinese characters to reduce variations in shape that are caused by variations in user handwriting. We therefore used nonlinear normalization to adjust the size of the characters by constraining their dimensions to a range of 32×32 (i.e., in which the range of X and Y coordinates was fixed to 32, as shown in Fig. 5b). Next, to reduce interpretation issues created by discrepancies in the number of coordinates collected due to writing speed, we performed a linear interpolation of Chinese character coordinates, as shown in Fig. 5c. Previous studies have shown significant improvement in the classification accuracy of handwritten Chinese characters following nonlinear normalization [48]. The most commonly used method for extracting the directional features of handwritten characters is the eight-directional vector method [49], which divides a 360° range into eight equally-spaced directional vectors. A diagram of an eight-directional vector is shown in Fig. 5d, while the eight-directional vector data collected here are shown in Fig. 5e. The red circles of the Chinese characters shown in the figure contain the two coordinates (x_0, y_0), (x_1, y_1). The projection to D1 is assumed to be a_1, the projection to D8 is assumed to be a_8, and the projection of the directional line onto all other directional vectors is assumed to be 0. The eight-directional feature values of a line segment in that direction can be written as $f = (a_1, 0, 0, 0, 0, 0, 0, a_8)$. We were then able to obtain eight-directional feature values for each of the coordinates of the Chinese characters analyzed here. In addition, Figs. 5f–5h show the eight-directional feature maps obtained for the Chinese character "ah" in the three directions. Other feature maps can be seen in Fig. S8 (Supplementary Information).

The design of a flexible touch-sensitive screen interaction system

Using the eight-directional vector method, we were then able to extract the feature maps of handwritten Chinese characters in eight directions. These eight feature maps (all 32×32 in size) could then be used as an input source for a convolutional neural network. The closer the value of a point in an eight-directional feature map is to 1, the better the overlap between the directional line segment and the directional vector at that point. The structure of the convolutional neural network configured in this work is shown in Fig. 6a. Here, we used a transfer learning strategy that involved a pre-trained few-shot learning model to obtain the initialization parameters for a convolutional neural network. The aim of transfer learning is to take the knowledge learned in one environment to assist in learning tasks in a new environment [50]. To implement this strategy, we first reduced the classification categories of Chinese characters and classified the first 20 characters of GB2312. Since all 3755 characters were extracted as eight-directional features, the convolutional neural network trained by this few-shot classification task was able to perform other kinds of feature extraction using the eight-directional feature map. Therefore, the convolutional neural network trained by this few-shot classification task was able to provide suitable initialization parameters for a convolutional neural network that could recognize 3755 Chinese characters. We note that the convolutional neural network model used for the few-shot classification task has the same structure and configuration as the convolutional neural network in Fig. 6a, except that the final layer had only 20 outputs. Next, we used the convolutional neural network parameters of the small classification task to initialize the convolutional neural network to recognize all handwritten Chinese characters.

We used the CASIA-OLHWDB 1.1 and ICDAR-2013 handwriting databases as whole samples and divided each into a training set (898,573 samples), a validation set (898,573 samples), and a test set (224,419 samples, ICDAR-2013). The loss values and accuracy of the validation set

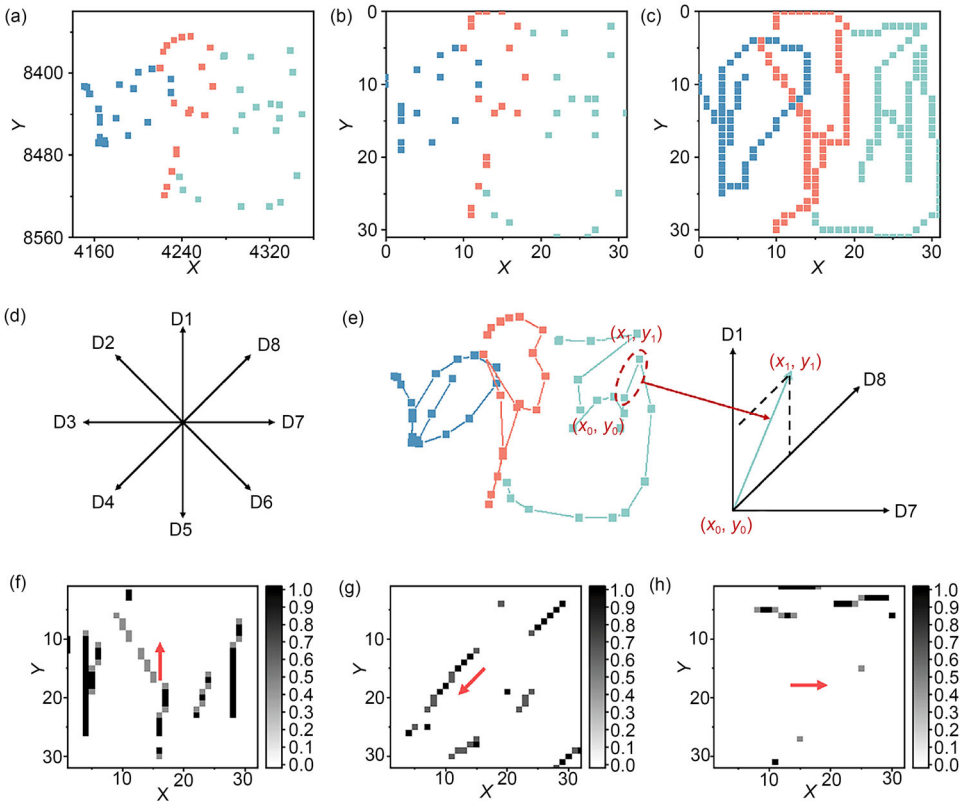

Fig. 5 **a** Original coordinate map of Chinese characters. For handwritten Chinese characters captured online, what the system generally captures is only its sparse set of coordinates. It is therefore difficult to determine which Chinese character these coordinates correspond to based on looking at raw data. **b**, **c** Images of the Chinese character "ah" following nonlinear normalization and linear interpolation, respectively. **d** An eight-directional vector. Each is divided at an angle of 45° in two directions. **e** Schematic diagram of the eight-directional decomposition of a line segment used in a Chinese character. **f**–**h** Three directions of the eight-directional feature maps used to characterize the Chinese character "ah"

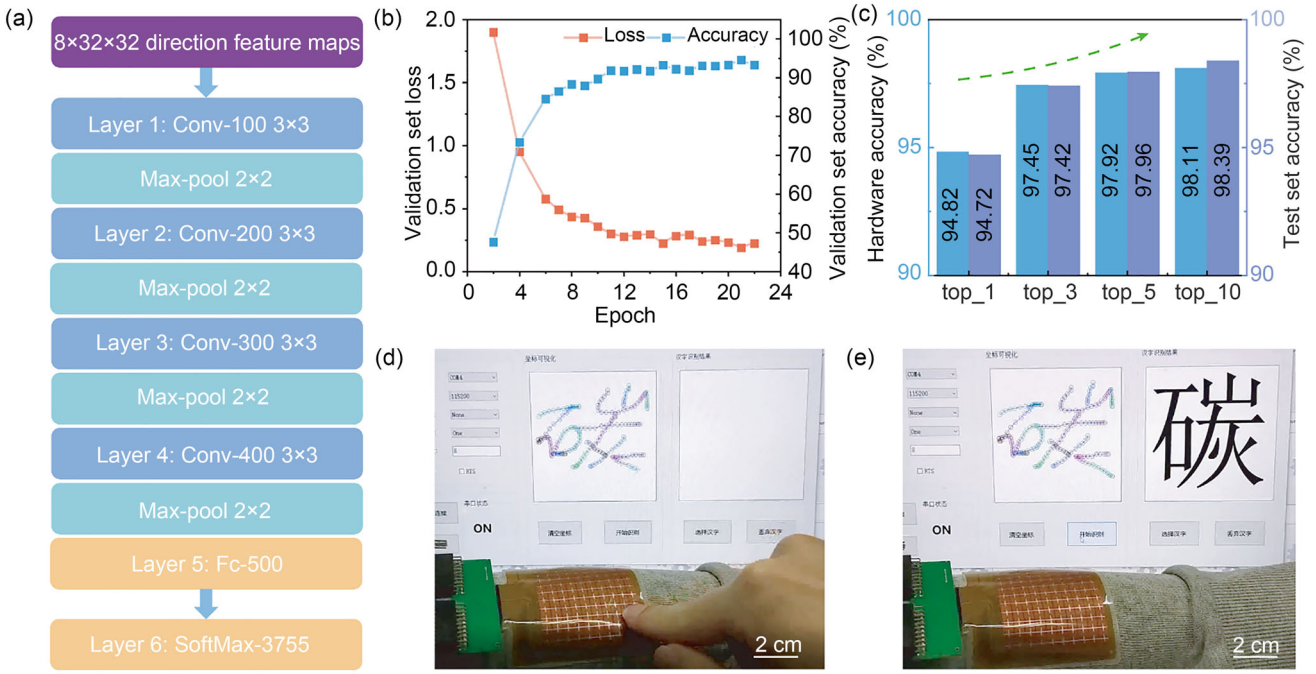

Fig. 6 **a** Convolutional neural network structure for handwritten Chinese character recognition. **b** Loss and accuracy of the validation set during 22 epochs of convolutional neural network following initialization to the parameters of the few-shot classification task. **c** The top-*K* accuracy of the convolutional neural network model on the test set and on the hardware of the flexible touch screen interaction system. **d** Usage of the flexible touch-sensitive screen interaction system. **e** The result of recognition. This Chinese character means "carbon"

during 22 epochs are shown in Fig. 6b. Moreover, the accuracy of this neural network reached 94.57%. Importantly, the loss value of the convolutional neural network did not experience further decreases in subsequent epochs, and the model converged. The top-*K* recognition accuracy of the test set (i.e., ICDAR-2013) is shown in Fig. 6c. Moreover, the hardware accuracy of the flexible touch interaction system in writing 600 given Chinese characters is shown in Fig. 6c. The high top-*K* accuracy means that the likelihood of recognizing which Chinese character is written by a user is greatly increased, which ensures that the flexible touch screen interaction system can work consistently.

The flexible touch-sensitive screen interaction system was then connected to a host computer as shown in Fig. 6d. As can be seen, the flexible touch-sensitive screen adhered well to the garment and bent with it. Next, when Chinese characters were handwritten on the screen, the host computer can display the touch coordinates in real time and connect the coordinates within the same stroke (Video S1 in Supplementary Information). Figure 6e shows the overall recognition results as implemented using this system: the Chinese character shown means "carbon." This matches the Chinese character written by the user and shows that the system can work accurately.

Conclusions

In this work, we propose a one-step method for the direct fabrication of induced charge-based mutual capacitive sensors. To do so, we implement an ECR system to deposit GMNFs on flexible substrates. By sputtering the material directly onto the substrate in the form of atoms, this method can effectively avoid problems caused by poor adhesion of the sensing material to the substrate. Moreover, it can reduce the fabrication and material costs involved in creating flexible touch sensors. The high precision of the sensor reported here is enabled by electron trapping and polarization effects of the mixed-coordinated bonding between copper nanoparticles and vertically grown graphene nanosheets. Next, we tested the performance of the touch-sensitive screen composed of GMNFs and found that the screen maintained high stability under a variety of test conditions. Furthermore, the screen interaction system was found to have an SNR of 41.16 dB and a resolution of up to 650 dpi. We then used it to test handwritten Chinese character recognition, where it achieved 94.82% accuracy. Overall, this work provides a new method for the direct fabrication of flexible sensors and illustrates the potential of GMNFs for wearable device applications.

Supplementary Information The online version contains supplementary material available at https://doi.org/10.1007/s42242-024-00293-3.

Acknowledgements This work was supported by the National Natural Science Foundation of China (Nos. 52275565, 52105593, and 62104155), the Natural Science Foundation of Guangdong Province, China (No. 2022A1515011667), the Shenzhen Foundation Research Key Project (No. JCYJ20200109114244249), the Youth Talent Fund of Guangdong Province, China (No. 2023A1515030292), and the Shenzhen Excellent Youth Basic Research Fund (No. RCYX20231211090249068). The authors wish to acknowledge the assistance with TEM/FIB received from the Electron Microscope Center of Shenzhen University.

Author contributions XZ, QW, BW, and DFD generated the concept and involved in writing the manuscript. JCM and HLD performed the experiments, collected data, conducted data analysis, and wrote the manuscript. JMZ and KCX helped in conducting experiments, data analysis, and statistical analysis. All authors have given approval to the final version of the manuscript.

Declarations

Conflict of interest This paper is to be included in a special issue for which KCX is a guest editor. CKX is also an academic editor for *Bio-Design and Manufacturing*. He was not involved in the editorial review or the decision to publish this article. The authors declare that they have no conflict of interest.

Ethical approval This article does not contain any studies with human or animal subjects performed by any of the authors.

References

1. Han SJ, Liu CR, Xu HH et al (2018) Multiscale nanowire-microfluidic hybrid strain sensors with high sensitivity and stretchability. npj Flex Electron 2(1):16. https://doi.org/10.1038/s41528-018-0029-x
2. Lee J, Kwon H, Seo J et al (2015) Conductive fiber-based ultrasensitive textile pressure sensor for wearable electronics. Adv Mater 27(15):2433–2439. https://doi.org/10.1002/adma.201500009
3. Lu YY, Yang G, Wang SQ et al (2024) Stretchable graphene–hydrogel interfaces for wearable and implantable bioelectronics. Nat Electron 7:51–65. https://doi.org/10.1038/s41928-023-01091-y
4. Chen WF, Yan X (2020) Progress in achieving high-performance piezoresistive and capacitive flexible pressure sensors: a review. J Mater Sci Technol 43:175–188. https://doi.org/10.1016/j.jmst.2019.11.010
5. Gao X, Zheng MP, Yan XD et al (2019) The alignment of BCZT particles in PDMS boosts the sensitivity and cycling reliability of a flexible piezoelectric touch sensor. J Mater Chem C 7(4):961–967. https://doi.org/10.1039/c8tc04741c
6. Zhang YR, Jen YH, Mo CT et al (2020) Realization of multistage detection sensitivity and dynamic range in capacitive tactile sensors. IEEE Sens J 20(17):9724–9732. https://doi.org/10.1109/Jsen.2020.2992484
7. Cui SY, Lu YY, Kong DP et al (2023) Laser direct writing of Ga_2O_3/liquid metal-based flexible humidity sensors. Opto-Electron Adv 6(7):220172. https://doi.org/10.29026/oea.2023.220172
8. Kim SJ, Phung TH, Kim S et al (2020) Low-cost fabrication method for thin, flexible, and transparent touch screen sensors. Adv Mater Technol 5(9):2000441. https://doi.org/10.1002/admt.202000441
9. Ziaei S, Wu Q, Fitch J et al (2019) Channel cracking and interfacial delamination of indium tin oxide (ITO) nano-sized films on

polyethylene terephthalate (PET) substrates: experiments and modeling. Exp Mech 59(5):703–712. https://doi.org/10.1007/s11340-019-00534-y
10. Wang X, Xiong Z, Liu Z et al (2015) Exfoliation at the liquid/air interface to assemble reduced graphene oxide ultrathin films for a flexible noncontact sensing device. Adv Mater 27(8):1370–1375. https://doi.org/10.1002/adma.201404069
11. Fu X, Zhang JQ, Xiao JL et al (2021) A high-resolution, ultrabroad-range and sensitive capacitive tactile sensor based on a CNT/PDMS composite for robotic hands. Nanoscale 13(44):18780–18788. https://doi.org/10.1039/d1nr03265h
12. Zhang ZA, Gui XC, Hu QM et al (2021) Highly sensitive capacitive pressure sensor based on a micropyramid array for health and motion monitoring. Adv Electron Mater 7(7):2100174. https://doi.org/10.1002/aelm.202100174
13. Zhang JQ, Wan LJ, Gao Y et al (2019) Highly stretchable and self-healable MXene/polyvinyl alcohol hydrogel electrode for wearable capacitive electronic skin. Adv Electron Mater 5(7):1900285. https://doi.org/10.1002/aelm.201900285
14. Hu WL, Niu XF, Zhao R et al (2013) Elastomeric transparent capacitive sensors based on an interpenetrating composite of silver nanowires and polyurethane. Appl Phys Lett 102:083303. https://doi.org/10.1063/1.4794143
15. Cheng L, Qian JC, Ruan DQ et al (2023) Flexible and highly sensitive sandwich-structured PDMS with silver nanowires and laser-induced graphene for rapid residue detection. ACS Appl Polym Mater 5(4):2336–2344. https://doi.org/10.1021/acsapm.2c02011
16. Wan YB, Qiu ZG, Hong Y et al (2018) A highly sensitive flexible capacitive tactile sensor with sparse and high-aspect-ratio microstructures. Adv Electron Mater 4(4):1700586. https://doi.org/10.1002/aelm.201700586
17. Chen WQ, Xiao PS, Chen HH et al (2019) Polymeric graphene bulk materials with a 3D cross-linked monolithic graphene network. Adv Mater 31(9):1802403. https://doi.org/10.1002/adma.201802403
18. Lee C, Wei XD, Kysar JW et al (2008) Measurement of the elastic properties and intrinsic strength of monolayer graphene. Science 321(5887):385–388. https://doi.org/10.1126/science.1157996
19. Akhavan O, Ghaderi E, Shirazian SA et al (2016) Rolled graphene oxide foams as three-dimensional scaffolds for growth of neural fibers using electrical stimulation of stem cells. Carbon 97:71–77. https://doi.org/10.1016/j.carbon.2015.06.079
20. Gu SY, Hsieh CT, Lin TW et al (2018) Atomic layer oxidation on graphene sheets for tuning their oxidation levels, electrical conductivities, and band gaps. Nanoscale 10(33):15521–15528. https://doi.org/10.1039/c8nr04013c
21. Nazarloo AS, Ahmadian MT, Firoozbakhsh K (2019) On the mechanical characteristics of graphene nanosheets: a fully nonlinear modified morse model. Nanotechnology 31(11):115708. https://doi.org/10.1088/1361-6528/ab598e
22. López V, Sundaram RS, Gómez-Navarro C et al (2009) Chemical vapor deposition repair of graphene oxide: a route to highly-conductive graphene monolayers. Adv Mater 21(46):4683–4686. https://doi.org/10.1002/adma.200901582
23. Qin J, Yin LJ, Hao YN et al (2021) Flexible and stretchable capacitive sensors with different microstructures. Adv Mater 33(34):2008267. https://doi.org/10.1002/adma.202008267
24. Yang J, Luo S, Zhou X et al (2019) Flexible, tunable, and ultrasensitive capacitive pressure sensor with microconformal graphene electrodes. ACS Appl Mater Interfaces 11(16):14997–15006. https://doi.org/10.1021/acsami.9b02049
25. Luo S, Yang J, Song XF et al (2018) Tunable-sensitivity flexible pressure sensor based on graphene transparent electrode. Solid-State Electron 145:29–33. https://doi.org/10.1016/j.sse.2018.04.003
26. Zhang Y, Yang JL, Hou XY et al (2022) Highly stable flexible pressure sensors with a quasi-homogeneous composition and interlinked interfaces. Nat Commun 13(1):1317. https://doi.org/10.1038/s41467-022-29093-y
27. Chen SC, Wang YF, Yang L et al (2020) Electron-induced perpendicular graphene sheets embedded porous carbon film for flexible touch sensors. Nano-Micro Lett 12(1):136. https://doi.org/10.1007/s40820-020-00480-8
28. Zhang X, Ma JC, Huang WH et al (2023) Direct fabrication of flexible tensile sensors enabled by polariton energy transfer based on graphene nanosheet films. Nanotech Precis Eng 6:013001. https://doi.org/10.1063/10.0016758
29. Zhang X, Tian LL, Diao DF (2021) High-response heterojunction phototransistor based on vertically grown graphene nanosheets film. Carbon 172:720–728. https://doi.org/10.1016/j.carbon.2020.10.054
30. Sarakinos K, Alami J, Konstantinidis S (2010) High power pulsed magnetron sputtering: a review on scientific and engineering state of the art. Surf Coat Technol 204(11):1661–1684. https://doi.org/10.1016/j.surfcoat.2009.11.013
31. Liu WJ, Liu R, Yu PF et al (2015) Device/circuit mixed-mode simulations for analysis and design of projected-capacitive touch sensors. J Disp Technol 11(2):204–208. https://doi.org/10.1109/Jdt.2014.2370453
32. Lyu C, Wen B, Bai YZ et al (2023) Bone-inspired (GNEC/HAPAAm) hydrogel with fatigue-resistance for use in underwater robots and highly piezoresistive sensors. Microsyst Nanoeng 9(1):99. https://doi.org/10.1038/s41378-023-00571-7
33. Chen Y, Li N, Hoagland RG et al (2020) Effects of three-dimensional Cu/Nb interfaces on strengthening and shear banding in nanoscale metallic multilayers. Acta Mater 199:593–601. https://doi.org/10.1016/j.actamat.2020.08.019
34. Yoo SJ, Kim CY, Shin JW et al (2013) Characterization of an amorphous carbon film covering a Mo grid during in situ heating TEM study. Mater Charact 78:31–36. https://doi.org/10.1016/j.matchar.2013.01.011
35. Devaraj S, Munichandraiah N (2008) Effect of crystallographic structure of MnO_2 on its electrochemical capacitance properties. J Phys Chem C 112(11):4406–4417. https://doi.org/10.1021/jp7108785
36. Ferrari AC, Robertson J (2000) Interpretation of Raman spectra of disordered and amorphous carbon. Phys Rev B 61(20):14095–14107. https://doi.org/10.1103/PhysRevB.61.14095
37. Lin ZZ, Hirao H, Sun CQ et al (2020) C–H oxidation enhancement on a gold nanoisland by atomic-undercoordination induced polarization. Phys Chem Chem Phys 22(26):14458–14464. https://doi.org/10.1039/d0cp01117g
38. Sun CQ, Wang Y, Nie YG et al (2009) Adatoms-induced local bond contraction, quantum trap depression, and charge polarization at Pt and Rh surfaces. J Phys Chem C 113(52):21889–21894. https://doi.org/10.1021/jp908220a
39. Thoresen CB, Hanke U (2017) Numerical simulation of mutual capacitance touch screens for ungrounded objects. IEEE Sens J 17(16):5143–5152. https://doi.org/10.1109/Jsen.2017.2721743
40. Zhao J, He CL, Yang R et al (2012) Ultra-sensitive strain sensors based on piezoresistive nanographene films. Appl Phys Lett 101(6):063112. https://doi.org/10.1063/1.4742331
41. Zhu LF, Wang YC, Mei DQ et al (2020) Fully elastomeric fingerprint-shaped electronic skin based on tunable patterned graphene/silver nanocomposites. ACS Appl Mater Interfaces 12(28):31725–31737. https://doi.org/10.1021/acsami.0c09653
42. Kwon OK, An JS, Hong SK (2018) Capacitive touch systems with styli for touch sensors: a review. IEEE Sens J 18(12):4832–4846. https://doi.org/10.1109/Jsen.2018.2830660

43. An JS, Ra JH, Kang E et al (2021) A readout IC for capacitive touch screen panels with 33.9 dB charge-overflow reduction using amplitude-modulated multi-frequency excitation. IEEE J Solid-State Circ 56(11):3486–3498. https://doi.org/10.1109/Jssc.2021.3100470
44. Kim HK, Lee S, Yun KS (2011) Capacitive tactile sensor array for touch screen application. Sens Actuat A 165(1):2–7. https://doi.org/10.1016/j.sna.2009.12.031
45. Zhang X, Lin ZZ, Peng D et al (2019) Edge-state-enhanced ultra-high photoresponsivity of graphene nanosheet-embedded carbon film/silicon heterojunction. Adv Mater Interfaces 6(11):1802062. https://doi.org/10.1002/admi.201802062
46. Zhang X, Peng D, Lin ZZ et al (2019) Edge effect on the photodetection ability of the graphene nanocrystallites embedded carbon film coated on p-silicon. Phys Status Solidi-Rapid Res Lett 13(6):1800511. https://doi.org/10.1002/pssr.201800511
47. Gao SY, Liu L, Lin ZZ et al (2021) High photoresponsivity of vertical graphene nanosheets/P–Si enhanced by electron trapping at edge quantum wells. J Phys Chem C 125(9):5392–5398. https://doi.org/10.1021/acs.jpcc.1c00137
48. Liu CL, Marukawa K (2005) Pseudo two-dimensional shape normalization methods for handwritten Chinese character recognition. Patt Recogn 38(12):2242–2255. https://doi.org/10.1016/j.patcog.2005.04.019
49. Ghosh T, Sen S, Obaidullah SM et al (2022) Advances in online handwritten recognition in the last decades. Comput Sci Rev 46:100515. https://doi.org/10.1016/j.cosrev.2022.100515
50. Zhuang FZ, Qi ZY, Duan KY et al (2021) A comprehensive survey on transfer learning. Proc IEEE 109(1):43–76. https://doi.org/10.1109/Jproc.2020.3004555